metals

MDPI

Article

Structure and Formation Model of Ag/TiO_2 and Au/TiO_2 Nanoparticles Synthesized through Ultrasonic Spray Pyrolysis

Gözde Alkan [1,*], Rebeka Rudolf [2], Jelena Bogovic [1], Darja Jenko [3] and Bernd Friedrich [1]

1 IME Process Metallurgy and Metal Recycling, RWTH Aachen, 52056 Aachen, Germany; jelena.bogovic@vtu.com (J.B.); bfriedrich@ime-aachen.de (B.F.)
2 Faculty of Mechanical Engineering, University of Maribor, 2000 Maribor, Slovenia; rebeka.rudolf@um.si
3 Institute of Metals and Technology, 1000 Ljubljana, Slovenia; darja.jenko@imt.si
* Correspondence: galkan@ime-aachen.de; Tel.: +49-241-80-95-873

Received: 31 July 2017; Accepted: 18 September 2017; Published: 25 September 2017

Abstract: This article explains the mechanism of the metal/oxide core-shell Ag/TiO_2 and Au/TiO_2 nanoparticle formation via one-step ultrasonic spray pyrolysis (USP) by establishing a new model. The general knowledge on the standard "droplet-to-particle" (DTP) mechanism, nucleation, and growth processes of noble metals, as well as physical and chemical properties of core and shell materials and experimental knowledge, were utilized with the purpose of the construction of this new model. This hypothesis was assessed on silver (Ag)/titanium oxide (TiO_2) and gold (Au) TiO_2 binary complex nanoparticles' experimental findings revealed by scanning electron microscopy (SEM), focused ion beam (FIB), high-resolution transmission electron microscopy (HRTEM), and simulation of crystal lattices. It was seen that two mechanisms run as proposed in the new model. However, there were some variations in size, morphology, and distribution of Ag and Au through the TiO_2 core particle and these variations could be explained by the inherent physical and chemical property differences of Ag and Au.

Keywords: ultrasonic spray pyrolysis; core shell nanostructure; formation mechanism; TiO_2; Ag; Au

1. Motivation and Background

Core shell complex nanostructures comprised of binary systems have been the focus of great interest due to their high functionality [1,2]. Preserving the core material's properties and modifying the surface with another material multiplies properties and, owing to the core/shell interface, superior performance has been introduced to a system that cannot be achieved by a single constituent. In recent studies, it was seen that thin surface layers on fine particles affect various properties substantially, such as chemical and thermal stability [3], catalytic activity [4], optical, magnetic, and electrical properties [5–8].

Among various combinations of materials that have been utilized as core-shell systems this study targets on inorganic-inorganic group of Ag/TiO_2 and Au/TiO_2. TiO_2 is proposed as a core material due to its inertness, chemical stability, and non-toxic nature [9]. It is a crystalline material with three polymorphic phases; anatase (tetragonal), rutile (tetragonal), brookite (orthorhombic), with an order of enthalpy of formation as; ΔH_f (rutile) < ΔH_f (brookite) < ΔH_f (anatase) [10,11]. Regarding the energetics of three polymorphs, rutile is the most stable phase, thermodynamically. However, these three compounds have a surface energy order as; Υ (anatase) < Υ (brookite) < Υ (rutile) Due to the fact that the surface energy becomes dominant in finer particles, different TiO_2 polymorphs can be synthesized depending on particle size. It was previously reported that the formation of fine anatase crystals via nucleation from solution is thermodynamically more favorable then rutile [12]. It is

crucial to consider the importance of the size, morphology and crystal form of TiO_2 on its properties and performance. Furthermore, TiO_2 is preferred commonly as core material for noble metal shells (e.g., Ag and Au) owing to its improved photocatalytic and antimicrobial properties [13,14]. In order to have control over the final microstructure it is important to understand the formation mechanism of these complex nanoparticles, which is led by nucleation and growth. Different nucleation behavior was reported of noble metals on different TiO_2 polymorphs [15–17]. Lai et al. [15] studied the most stable surface (1 1 0) of rutile which includes five-fold coordinated Ti atoms rows and two-fold coordinated bridging O atoms. It was found out that nucleation of metal nanoclusters initiated at surface defects, which is thermodynamically favorable due to the high adsorption energy and Ti cation sites between bridging oxygen rows [16]. On the other hand, the most stable surface of anatase is reported by Vittadini et al. [17], as (1 0 1) which serves five-fold coordinated O anions and five-fold coordinated Ti atoms as mostly preferential nucleation sites of noble metal clusters. Moreover, the importance was also emphasized of stoichiometric or defected types of anatase. In stochiometric anatase, the formation of isolated Au clusters that connect to the surface and O atoms is proposed, while oxygen deficiency induces wetting behavior of the metal cluster by acting as a nucleation site in the defected anatase. Regarding this knowledge, it can be said that the crystal structure and surface properties of TiO_2, which are highly related with USP process parameters, are playing a crucial role in the nucleation manner of nanoclusters and, therefore, on the final microstructure. After nucleation, 2D, quasi 2D and 3D growth of these clusters take place, respectively. The equilibrium shape of a cluster is determined by the balance of the forces between the surface and the interfacial energy. Isotropy of clusters varies the mechanism as given in Figure 1 [16].

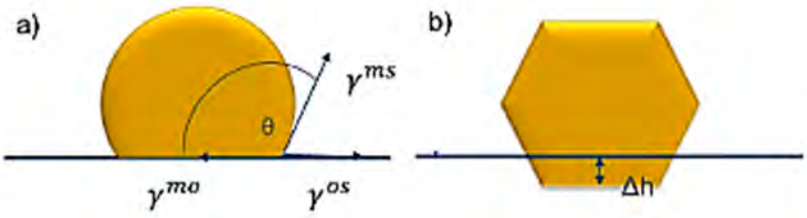

Figure 1. Schematic representation of an equilibrium cluster (**a**) Isotropic surface, γ^{ms} and γ^{os} are metal and oxide surface energy, and γ^{mo} is the interfacial energy between the metal and oxide; (**b**) anisotropic surface and faceted shape (Wulff construction); the cluster is truncated into oxide (Δh), which is dependent on the cluster surface energy and adhesion energy; Reproduced with permission from [16], World Scientific, 2001.

When the cluster is isotropic, a spherical shape is obtained which has a contact angle with the surface. This angle is a measure of the wetting ability and a function of the surface energy of the metal, surface energy of titanium oxide and surface energy of the interface. In the case of high metal and metal oxide surface energy, thin film growth is favored on the surface. However, when the cluster is anistropic (interfacial energy depends on direction), the shape of the crystal at equilibrium is determined by Wulff construction based on evaluating surface tension as a function of interface orientation [18]. Furthermore, Galhenage et al. [19] discussed the relevance of metal cluster growth behaviour on their thermodynamical properties. It was pointed out that, with decreasing metal-oxygen bond strength, the diffusion rates of metal increase, which causes larger agglomerated clusters away from the target thin film growth. Since all metals have unique interaction with the TiO_2 surface, the final microstructure varies with metal type. This indicates the importance of metal selection on the final morphology of the core-shell structure.

In summary, the surface and crystallographic properties of TiO_2 core and noble metals and metal-TiO_2 interface properties play a huge role in the final core-shell microstructure. Consistent with that fact, the differences and similarities between Ag/TiO_2 and Au/TiO_2 nanoparticles synthesized by USP presented in our previous report [20], formed the platform of a detailed investigation to

explain the formation mechanism of these systems considering the material properties of core and shell materials and USP process parameters. The most remarkable findings of our previous study can be summarized as; they exhibited more or less the same morphology, with some variations in size, shape and distribution. SEM and TEM micrographs revealed that the size of the Au nanoparticles was much smaller than the size of the Ag nanoparticles (the Au nanoparticles were in the size range 7–50 nm, where most of the particles were around 10 nm in size, whereas the average size of the Ag nanoparticles ranged from around 20 nm to 80 nm). Moreover, Ag nanoparticles exhibited mostly an ideally-spherical shape (hexagonal in the case of the defect formation, twinning, etc.), whereas the Au nanoparticles had various forms from spherical and cylindrical to an irregular shape. In addition, FIB was performed to observe cross-sectional microstructures. In the case of the Ag/TiO_2 nanoparticles, almost all the Ag nanoparticles were formed on the oxide surface (>90%), whereas in the case of Au/TiO_2 nanoparticles, some of the Au nanoparticles were formed in the volume of the TiO_2 nanoparticles (30%) and distributed randomly in the oxide matrix. The origin of these variations in two noble metal/TiO_2 nanoparticles produced by the same process is still not clear and needs further investigation for explanation.

For this purpose, this study provides further detailed HRTEM micrographs, electron diffraction patterns and atomic simulation of the plane TiO_2 core, Ag/TiO_2 and Au/TiO_2, which revealed crystallographic interaction between the noble metals (Au, Ag) and the core surface. After that, a model was proposed by utilizing the theoretical knowledge of the droplet-to-particle theory (DTP), nucleation and growth mechanisms and previous experimental experiences [21–26]. Moreover, this newly-proposed model was validated by explaining the morphological and crystallographic differences revealed by previous and currently performed characterizations based on the different inherent physical, chemical, and crystallographic properties of two noble metals.

2. Experimental Methods

Tetra-n-butylorthotitanate $C_{16}H_{36}O_4Ti$ (Merck, Darmstadt, Germany); hydrogen tetrachloroaurate $HAuCl_4$ (A Johnson Matthey Company, Redwitz, Germany); and silver nitrate $AgNO_3$ commercial precursors were used as TiO_2, Au, and Ag precursors, respectively. De-ionized water was used for all solutions as the solvent. Since $C_{16}H_{36}O_4Ti$ is unstable in contact with water and hydrolyzes rapidly, it was stabilized with hydrochloric acid (HCl). For the precursor solutions for Ag and Au, a defined mass of $AgNO_3$ or $HAuCl_4$ was dissolved in de-ionized (DI) water. For core-shell synthesis, the prepared noble metal precursor solution was mixed in a defined ratio with the $C_{16}H_{36}O_4Ti$ solution. In the case of $AgNO_3/C_{16}H_{36}O_4Ti$ mixture, due to the instability of Ag ions in the presence of HCl, HNO_3, was used as a stabilizer. Since it is not thermodynamically favorable [27], oxidation of Au and Ag metals has not occurred during the USP process and they were found in the product in metal form.

The synthesis was performed with single-step USP equipment. The main equipment parts are carrier and/or reaction gas connected over the flow regulator (with the possibility to mix the carrier and reaction gas), the ultrasonic aerosol generator (2.5 MHz; Gapusol, RBI, Meylan, France), the horizontal furnace with a quartz tube reactor, and the collection of produced nanoparticles in the collection bottles.

Conventional transmission electron microscopy (CTEM), high-resolution TEM, and selective area electron diffraction (SAED) were performed using a Jeol JEM-2100 microscope (JEOL Ltd., Tokyo, Japan) operated at 200 kV accelerating voltage for observations of morphology of the nanoparticles. In addition, phase composition of the samples was determined using a Jeol JED-2300 Series energy dispersive spectrometer (EDS) (JEOL Ltd., Tokyo, Japan) attached to the TEM. FindIt (Version 1.9.6 2015-1, Fachinformationszentrum, Karlsruhe, Germany and National Institute of Standards and Technology, Gaithersburg, MD, USA), PCPDFWIN (Version 2.02, ICDD, Newtown Square, PA, USA), PowderX (Beta version, Institute of Physics, Chinese Academy of Science, Beijing, China), and CrystalMaker (Version 2.2.3, CrystalMaker Software Limited, Oxfordshire, UK) programs were used for the identification/characterization of spots in the electron diffraction patterns to determine the crystal structure, to perform the simulations, and for electron diffraction pattern identification.

3. Results of Structural Characterization and Discussion of the Formation Process

In order to propose a precise formation model for Ag/TiO_2 and Au/TiO_2 structures, it is important to understand pure TiO_2 for comparison purposes. Therefore, the pure TiO_2 core material that provides nucleation sites to noble metals were analyzed by transmission electron microscopy (TEM) and high-resolution transmission electron microscopy (HRTEM), presented in Figure 2, to reveal a stable crystal structure, orientation, surface features and defects which have control over the nucleation mode.

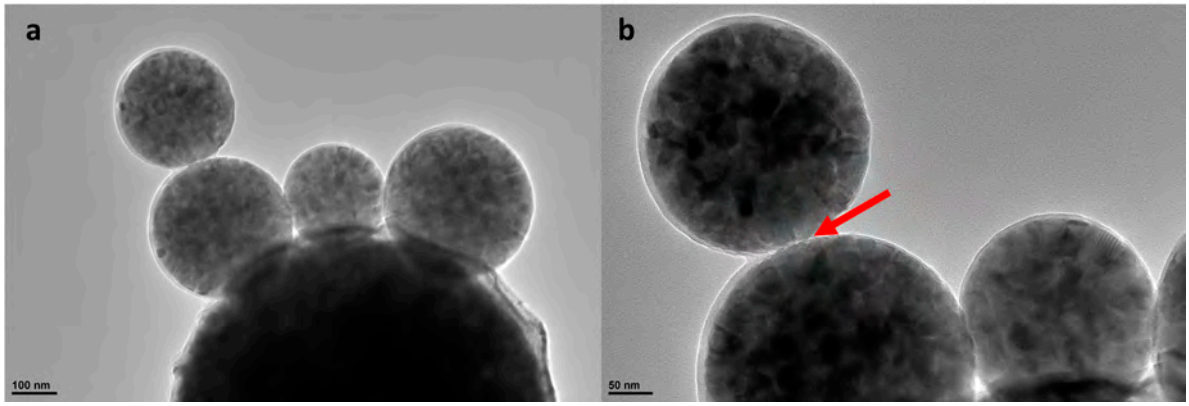

Figure 2. TEM analyze of the TiO_2: (**a**) spherical nanoparticles; and (**b**) detail showing that the individual nanoparticles are building the soft agglomerates (see arrow).

From Figure 2 it is easy to see that TiO_2 is present as secondary nanoparticles having varying sizes between 200 nm and 600 nm. When these secondary structures are investigated in detail, it can be seen that they are constructed by sintered primary small crystals with a size range of 5–20 nm. Moreover, TiO_2 secondary nanoparticles are observed as in both soft and hard agglomerates as shown in Figure 2a,b, respectively. When Figure 2a is considered, relatively smaller secondary particles of TiO_2 are found to be engraved to the bigger particle's surface. In contrast, Figure 2b reveals the soft agglomerates that are just in contact physically and can be separated easily by mechanical dispersion. Moreover, a high concentration of defects were also detected in the microstructure inherent from high reaction temperature and temperature gradient [27].

After having more insight information about the crystallinity and structure of TiO_2, the first core-shell system of Ag/TiO_2 were characterized by HRTEM. The results of the structural analyze of the multicomponent nanoparticles of Ag/TiO_2, the electron diffraction patterns and atomic simulations are represented in Figure 3.

From the results presented in Figure 3, it can be observed that the TiO_2 nanoparticles have spherical form with particle sizes in the range of 200–300 nm. Initial particles are partly visible (size below 50 nm), with their structure and grain boundaries as also revealed in the plane TiO_2 structure given in Figure 3. Since no concentration gradient can be observed the oxide nanoparticles seem to have a filled morphology. The silver nanoparticles are easy to spot and differentiate from the oxide primer particle by their color on the TEM micrograph. The silver nanoparticles are darker than the oxide, which is the consequence of sufficient density difference between silver and titanium dioxide (10.49 g/cm^3 for silver, 4.23 g/cm^3 for rutile and 3.78 g/cm^3 for anatase) as consistent with previous studies [28,29]. The Ag nanoparticles revealed in lower magnification (see Figure 3a,b) are observed mostly in spherical morphology. However, it is worth emphasizing that, when these silver nanoparticles on the TiO_2 surface were analyzed with higher magnification providing greater detail, it was found that they exhibit polygonal morphology, which was determined by Wullf's construction. Furthermore, the presence of structural defects can be observed in the structure of some particles (see Figure 3c).

In Figure 3e–g, comparison of electron diffraction patterns with simulated anatase, rutile, and brookite are given corresponding to points represented on the micrograph in Figure 3a as 1, 2, and 3, respectively. It is possible to see that the oxide nanoparticles labeled as 1 exhibit anatase structure, which is the TiO_2 polymorph with minimum surface energy [12]. It is possible to find some traces of brookite and rutile, in particles labeled 2 and 3, which are relatively finer, where the surface energy is not highly considerable. As mentioned before, in terms of enthalpy of formation value, the most stable phase of titania is rutile. However, TiO_2 synthesized by USP exhibited anatase and trace amounts of brookite phases. An explanation for this can be that the lower surface energy of anatase with respect to rutile becomes a dominant criterion over enthalpy of formation in the case of high surface area creation taking place and favoring the anatase polymorph in the presence of finer particles. Another scenario may be due to the fast nature of the USP process that does not allow enough time for diffusion and stable phase formation, which may result in metastable phase production. This allows synthesis products which it is not possible to obtain through conventional synthesis techniques, which, consequently, increases the importance of the USP method.

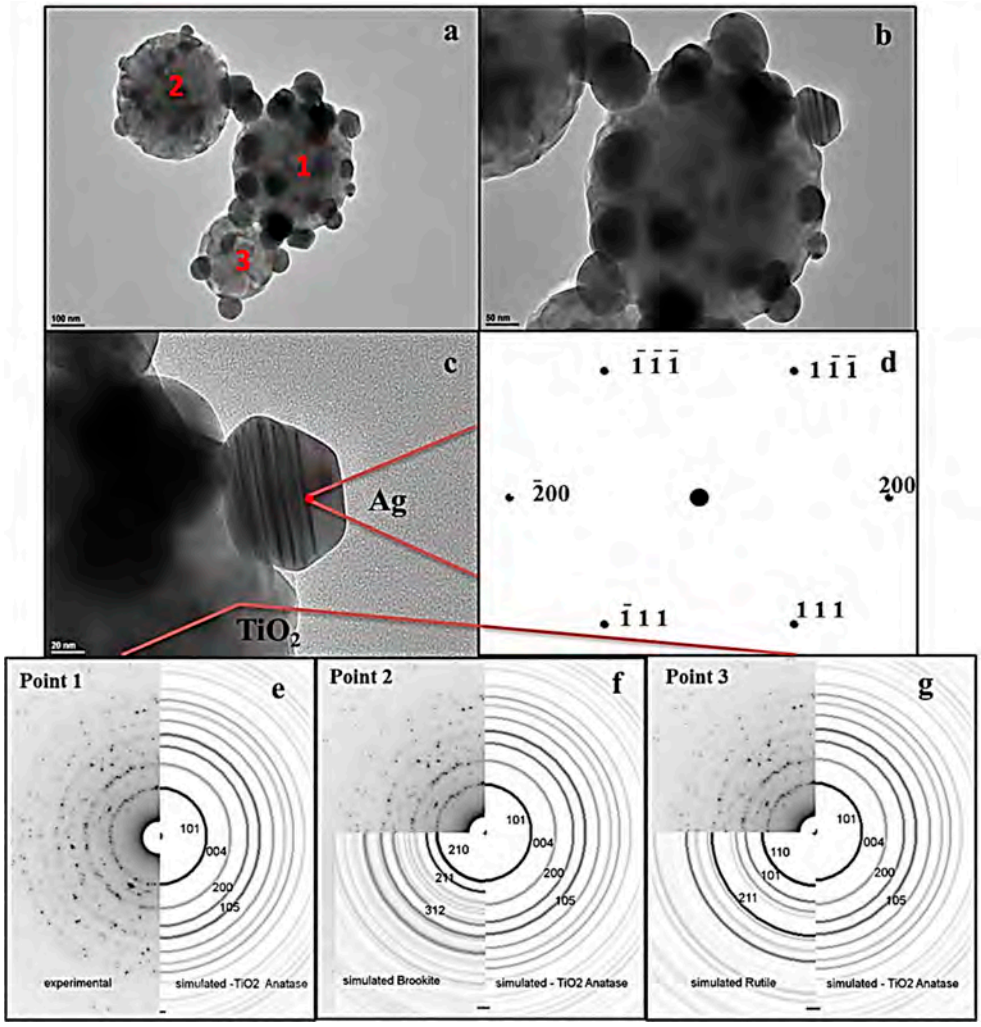

Figure 3. TEM micrographs of Ag/TiO_2 powder: (**a**) TiO_2 nanoparticles with the distributed Ag nanoparticles; (**b**) TiO_2 nanoparticles with partly-defined primary nanoparticles and clearly visible Ag nanoparticles; (**c**) Defect in Ag nanoparticle structure (twins); (**d**) simulation of the transmission electron diffraction for Ag in the [011] TiO_2 plane; electron diffraction patterns of Ag/TiO_2 powder from the upper image (**a**) where only a TiO_2 component was analyzed and simulated results for (**e**) anatase; (**f**) anatase and rutile; and (**g**) anatase and brookite.

An atomic simulation of the Ag/TiO_2 system is also provided which reveals the crystal structure in Figure 3d. From the diffraction rays in Ag in the [011] TiO_2 plane, the planes for each of the rings were calculated by using the program Crystal Maker. The calculation showed that it goes about the ccp (cubic close-packed) crystal structure (see Figure 3d), space group: Fm-3m (space group number: 225) typical for silver. From the literature [30] it is known that the cell parameters are: *a*: 408.53 pm, *b*: 408.53 pm, *c*: 408.53 pm, α: 90.000°, β: 90.000°, and γ: 90.000°.

In the next step, Au/TiO_2 complex nanoparticles were also examined in an identical manner in order to have a direct comparison between the two core-shell systems. HRTEM micrographs, electron diffraction patterns, and atomic simulation of Au/TiO_2 are shown in Figure 4.

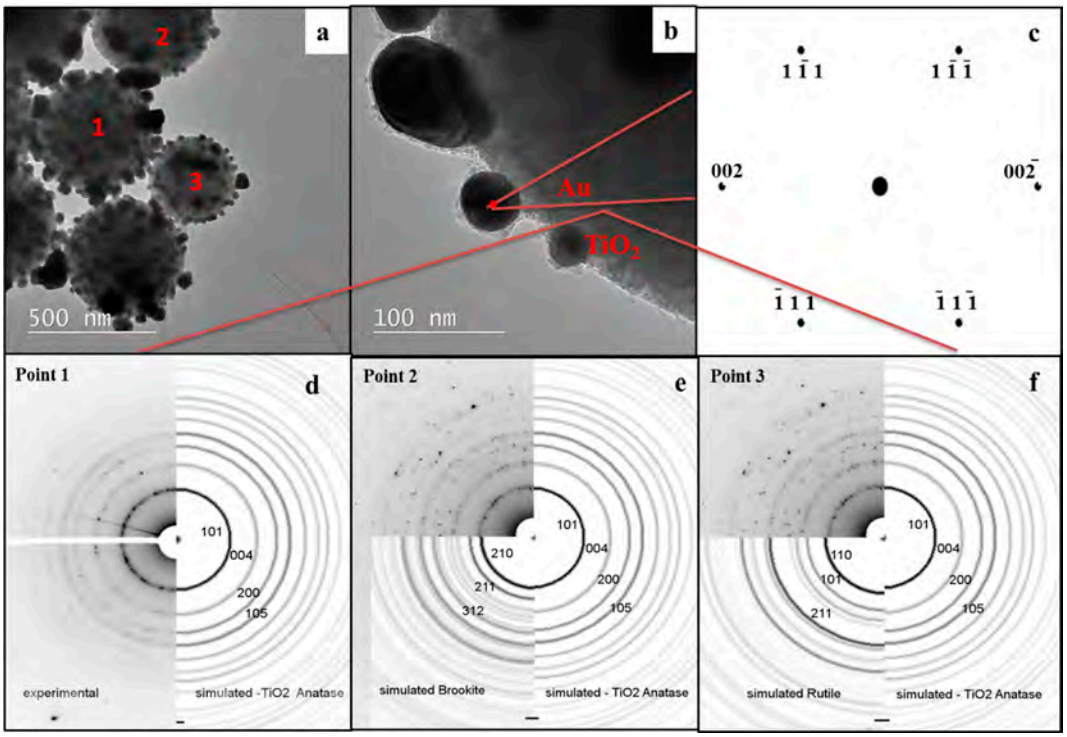

Figure 4. TEM micrographs of Au/TiO_2 powder: (**a**) polygonal (almost spherical) TiO_2 nanoparticle with distributed Au nanoparticles; (**b**) details of Au nanoparticles; (**c**) simulation of the transmission electron diffraction for Au in the [001] TiO_2 plane. Electron diffraction patterns of Au/TiO_2 powder where only a TiO_2 component was analyzed and simulated results for (**d**) anatase; (**e**) anatase and rutile; and (**f**) anatase and brookite.

TEM micrographs of Au/TiO_2 are represented in Figure 4. In order to provide a direct comparison between Ag and Au, the same magnifications were aimed to be used as the ones in Figure 3. However, TiO_2 nanoparticles in Au/TiO_2, which are around 500–600 nm, which is approximately two-fold coarser than the ones in the Ag/TiO_2 system, did not allow that. The relatively larger TiO_2 spheres are polycrystalline, formed from small units. Individual gold nanoparticles are distributed homogenously on the oxide surface. In contrast with Ag nanoparticles with a lower magnification, Au nanoparticles sized between 7 nm and 50 nm were observed with a dominating irregular morphology of granules and flakes. However, the higher magnification that can be seen in Figure 4b revealed that the Au nanoparticles exhibited mostly potato like spherical morphology distinct from the polygonal morphology of Ag. Figure 4b also reveals the engravement of gold nanoparticles to the TiO_2 core surface. Furthermore, the lattice fringes can be observed nicely on the high-resolution TEM, as well as the various defects and the growth of individual particles in the contact surface. Next to this, many defects can be found in the Au and TiO_2 which may be due to the high USP process temperature.

Beyond morphological findings, Figure 4d–f present the electron diffraction patterns for the TiO_2 crystal structure in the Au/TiO_2 core-shell system corresponding to points 1, 2, and 3, labeled in Figure 4a. These results are in parallel with the findings of Ag/TiO_2 systems represented in Figure 3. Mostly, larger TiO_2 particles exhibit anatase structure, where finer ones are detected in brookite and rutile forms, emphasizing the importance of the surface energy in the particle formation mechanism.

Moreover, atomic simulation of the Au/TiO_2 system is also provided which reveals the crystal structure in the simulation of the transmission electron diffraction for Au in the [001] TiO_2 plane.

From the diffraction rays in Au in the [001] TiO_2 plane, the planes for each of the rings were calculated by using the program Crystal Maker. The calculation showed that it goes about the ccp (cubic close-packed) crystal structure (see Figure 4c)—Space group: Fm-3m (space group number: 225) typical for gold. From the literature [30] it is known that the cell parameters are: *a*: 407.82 pm, *b*: 407.82 pm, *c*: 407.82 pm, α: 90.000°, β: 90.000°, and γ: 90.000°.

4. Formation Model and Validation

All the general knowledge for the USP process [31–33] can be transferred directly to the model for the noble metal/oxide particle formation. For these systems, an initial precursor solution with two components experience all the fundamental USP process steps, such as evaporation, precipitation, thermal decomposition, and drying; however, not at the same time-volume point for both components. In an ideal case, precursors do not react with each other so that, during the whole formation process, two separate components exist, undergoing the proposed formation steps and not having significant mutual influence on the precipitation in the droplet. A new formation model of an ideal core-shell nanoparticle was proposed according to these two assessed criteria. This theory is based on solute diffusion to the droplet surface and achieving a critical supersaturation concentration to nucleate. The start of nucleation was defined as the point where the components achieve supersaturation concentration. Although relatively lower precursor concentrations were used for obtaining nano-sized particles, evaporation of the solvent was utilized to bring the system to supersaturation. Then, the change in saturation concentration and position of metals and oxides in the dynamically-changing droplet/particle volume was proposed as a function of reaction time. In Figure 5, the proposed new model for the metal/oxide particle formation is presented, including different reaction times labeled as t_0, t', t'', t'''. The presented time points can be represented as the following relations: $t_0 < t' < t'' < t'''$ with their corresponding diameters R, R', R'', R'''; respectively. Relevant concentrations are abbreviated as follows: C_{crit_m} is the critical supersaturating concentration of the metallic precursor; C_{s_m} is the saturation concentration of the metallic precursor; C_{s_ox} is the saturation concentration of the oxide precursor; $C_{\_m}$, $C'_{\_m}$, $C''_{\_m}$, and $C'''_{\_m}$ are concentrations of the metallic precursor at the times t_0, t', t'', and t''', at corresponding droplet diameters R, R', R'', and R'''; $C_{\_ox}$, $C'_{\_ox}$, $C''_{\_ox}$, and $C'''_{\_ox}$ are concentrations of the oxide precursor at the times t_0, t', t'', and t''', at corresponding droplet diameters R, R', R'', and R'''.

A gradual decrease in the droplet/particle diameter (from R to R''') was observed as reaction propagates. Below each schematically-presented stage, there is a corresponding concentration profile through the droplet for the metal and oxide precursors. At the initial reaction time, which is shown as t_0, the corresponding droplet diameter is R, the droplet is in the liquid solution phase consisting of two precursors. After a certain time, which is shown as t', due to evaporation, the droplet diameter is reduced to R'. On the concentration diagram given below the schematic droplet it is possible to see that the concentration of the oxide precursor had reached the critical supersaturating concentration (C_{crit_ox}). The precipitation of the oxide component starts firstly on the already-existing droplet surface due to free energy concerns. Since the concentration of the metal precursor still did not reach the critical supersaturated concentration, the metal component diffused with the solvent to the droplet surface without any precipitation.

At a further reaction time t'', the corresponding droplet diameter decreased to R'' due to advanced evaporation. Moreover, at this stage of reaction, the on-going oxide precipitation moved through the

center while the metallic precursor had reached the critical supersaturating concentration (C_{crit_m}) so that the heterogeneous nucleation of the metal component on the already-existing oxide surface could take place. Since it is thermodynamically more favorable, the precipitation starts predominantly on the surfaces with lower effective surface energy, such as the grain boundary, defects, etc. At the last t''' point, almost all solvent evaporated and the droplet/particle had reached the R''' diameter. In the ideal case, all metallic precursors had succeeded in diffusing with the solvent to the droplet/particle surface and precipitated there. In the case that the precipitation front was moving faster than the diffusion front, some of the metal precipitation may also occur in the particle volume. This may occur at the relatively low value of C_{crit_m} or, in the case of very small droplets, due to solvent evaporation in the droplet/particle volume.

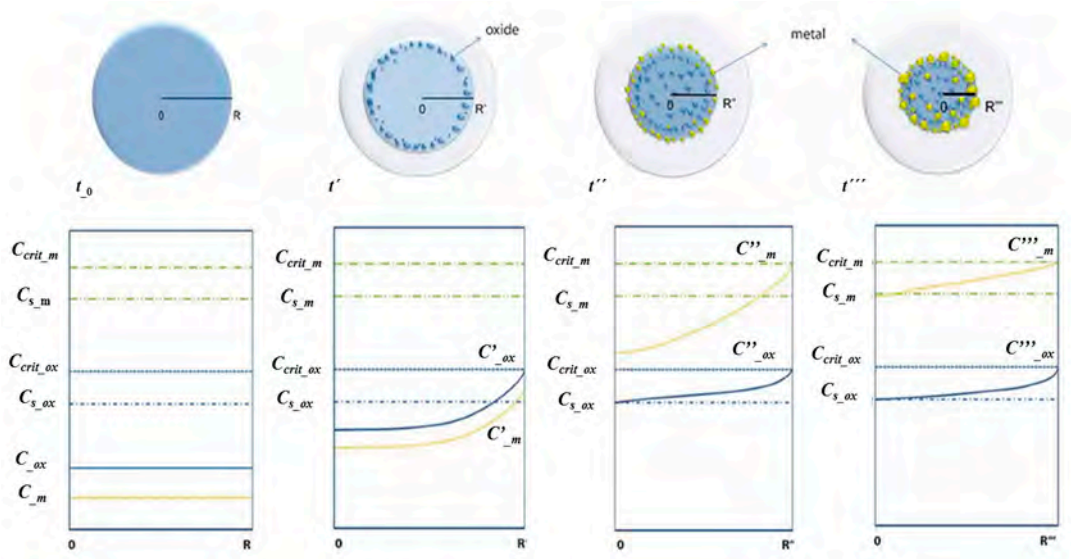

Figure 5. Proposed new model for metal/oxide nanoparticle formation by USP in one-step with the theoretical concentration gradient of oxides and metallic precursors in the droplet during the evaporation/precipitation process steps.

From the model presented in Figure 5 it is possible to see that the value of the critical supersaturating concentration of precursors plays an important role, because it is defining at which point the precipitation is going to take place. It is important to notice that the large difference in the solubility and separate precipitation of the oxide and metal components, running one after another, can be influenced in two ways: by varying the physical characteristics of the precursor (solubility) and the molar ratio of the precursor components in the starting solution, respectively. By looking at the proposed mechanisms to control the separate precipitation, it can be determined that the first one (solubility) is a constant for the chosen system and that it is only possible to change the second factor. This means that, in order to achieve the target metal/oxide morphology, based on the proposed model, it is important to have a concentration of metallic precursor lower than the concentration of the oxide precursor in the starting solution. In this way the component with the lower solubility and the higher concentration (the oxide in this case) is going to precipitate first and form the main volume of the oxide particle. After the evaporation/precipitation step completed, as in the proposed model, the classical D-T-P steps follow: reaction/decomposition, drying, densification stages. Previous studies have also reported the importance of relative concentrations of constituents to form the core-shell microstructure. Mädler et al. [27] utilized higher concentrations of SiO_2 and TiO_2 precursors for their fast precipitation and allowed gold to form on their surface in order to achieve Au/SiO_2 and Au/TiO_2 core shell structures by flame spray pyrolysis. Well dispersed fine Au particles on the surface of both oxides was achieved with this method. Another study performed by Nomoev et al. [34] aiming to

get Ag/Si core shell nanoparticles via one-step gas phase synthesis by electron beam evaporation also revealed the importance of concentration adjustment. Formation of the core shell structure was only achieved with an optimum Si/Ag ratio. These previous investigations are consistent with our proposed model emphasizing that higher metal oxide concentrations (80 wt % Ti precursor) provide early achievement of metal oxide to saturation and precipitation.

Thermal analyses of the Au and Ag precursors were considered in order to understand the thermal decomposition reaction step better. Next to the melting and decomposition point, the solubility of two metals was compared, which is the basis of the presented model (Figure 5). The summary of the most important physical characteristics of the Au and Ag precursors are presented in Table 1.

Table 1. Physical characteristics of Ag and Au precursors.

Precursor	Solubility of Metals [g/100 mL H_2O]	$T_{melting}$ [°C]	T_{Decomp} [°C]
$Ag^+ [NO_3]^-$	Ag → 234	212	444
$H^+ [AuCl_4]^-/Au^{+3} [Cl^-]_3$	Au → 68	254	>160
$Au^+ Cl^-$	Au → 3.1×10^{-5}	420 [35]	>289

The first main difference in the physical characteristics of precursors is their solubility in water. The silver nitrate has a 3.5 times higher solubility than the gold (III) chloride and a 7×10^6 time higher solubility than the gold (I) chloride. The morphological differences in the structure of Ag/TiO_2 and Au/TiO_2 nanoparticles are easy to explain with the listed physical property differences presented in Table 1.

The proposed scenario for the metal/oxide particle formation, in the case of the Ag and Au as the metallic components, is presented schematically in Figure 6.

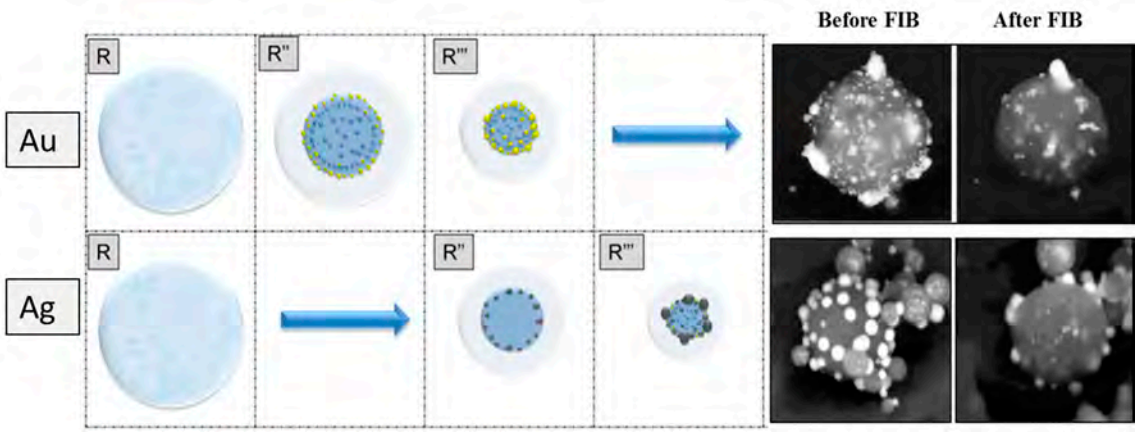

Figure 6. Schematic representation of the proposed new model for metal/oxide nanoparticle formation, applied on Ag/TiO_2 and Au/TiO_2 nanoparticles with the examples of the microstructural analyses confirmed before and after FIB milling [20].

As proposed in the model presented in Figure 5, the precipitation of solute (precursor) will start by reaching the critical supersaturating point. This concentration is reached by the increase of the initial concentration due to solvent evaporation, followed by droplet radius reduction from R to R''. Since $C_{crit\_AuCl3} < C_{crit\_AgNO3}$, the precipitation shall occur at $R''_{AuCl3} > R''_{AgNO3}$ (see Figure 6). The whole process takes place in the tube reactor, with a certain temperature profile, differentiating as a function of time and also location within the chamber. This means that the R''_{AuCl3} radius is going to be reached before the R''_{AgNO3} and at a lower temperature. The formation of the first crystals and the growth of noble metal occur firstly at the surface of the droplet, on the already formed initial particles of oxide, at the sites with the high adsorption energy (various defects that are acting as nucleation

centers). After this, the precipitation line moves towards the center of the droplet and the diffusion of the solute (precursor) continues from the droplet center towards the surface. Since the characteristic radius of the droplet in the precipitation point for Au and Ag stand in the relation $R''_{AuCl3} > R''_{AgNO3}$; the diffusion path of the Au precursor is also larger than in the case of Ag. In addition, the diffusion at the lower temperature is also slower. By reaching the characteristic radius R''', the rest of the precursor in the droplet center will also precipitate as presented in Figure 6. As the result of the combination of these factors, the Ag precursor can reach the droplet/particle surface better by diffusion before precipitating. This can be observed easily in the FIB analyze results presented in Figure 6 here, in the case of Ag/TiO_2, only a few very small particles of Ag are trapped in the TiO_2 volume. Details of FIB analyses can be found elsewhere [23]. These comparative results emphasize the importance of solubility for achieving good phase separation. In parallel, Deng et al. [36] have investigated the formation of Ru-Ni core shell nanoparticles via USP and reported the necessity of solubility difference between constituents. $RuCl_3$, which is hardly soluble in water, reached critical supersaturation earlier than $NiCl_2$ and precipitated to form the core of the product. The Ni precursor was precipitated on already-existing $RuCl_3$ surfaces and then both salts were decomposed to their bimetallic core shell structure, which follows the same reaction steps proposed by our new formation model.

Another dramatic difference observed between Au and Ag including core-shell systems is the size of the TiO_2 core material. While a size range of 200–300 nm was observed in the core material of Ag/TiO_2, it was detected in a range of 500–600 nm in Au/TiO_2. This two-fold increase in size may also be explained by the distribution of noble metals through the TiO_2. As revealed by FIB analyzes, a certain amount of Au was entrapped in the TiO_2 volume, while most of the Ag solutes reached the surface of the TiO_2 with minimized losses. The nucleation of the Ag nanoparticles on the TiO_2 surface may act like an obstacle for grain boundary movement that causes further grain growth and yields relatively lower sizes when compared with TiO_2 in Au/TiO_2 structure.

The proposed mechanism of the growth of Ag and Au nanoparticles on the oxide surface is presented in Figure 5 and it is the same for both metals. It starts with the formation of the "seeds" at the most preferable surface (the surface with the highest defect density, grain boundary, etc.), followed by initial growth that starts as a 2D growth and, after deposition of a monolayer, quasi-2D growth continues and transforms to 3D growth. At this point, it is important to notice the second obvious difference between the Ag and Au precursors. In the case of the $AgNO_3$, the melting point lies below the decomposition point which means that, after precipitation, the melting takes place. After reaching 444 °C, the decomposition can take place and the particle formation starts in the melt phase. In this decomposition type, appropriate crystal systems and orientations determined by Wullfs construction controls the equilibrium shape of the crystal, which explains the polygonal shape of the Ag nanoparticles revealed in Figure 3. On the other hand, Au formation follows the precipitation process, which always aims to minimize surface energy, and this explains the spherical morphology of Au nanoparticles in the core-shell structure. Moreover, it was reported [27] previously that during spray pyrolysis, gold droplets are exposed to high temperature gradient and may become highly supersaturated, which can cause homogenous precipitation of gold associating with heteregenous nucleation on top of oxide surfaces. Temperature gradient in this study was also high ($T_{reaction}$ = 800 °C, $T_{ambient}$ = 22 °C). These findings are coherent with Au spherical particles with minimized surface area. Beyond the considered physical and chemical properties of precursors, lattice mismatch between constituents is also critical to achieve the target morphology in core-shell structures. A theoretical prediction was performed utilizing lattice parameters of Ag (111), Au (111) and anatase (101) planes, since they were revealed majorly via the electronic difraction analyses presented in Figures 3 and 4. It was seen that lattice parameters of Ag and Au are very close, 4.0853 Å and 4.0782 Å, respectively [37]. The calculated lattice mismatch was 7.4% and 7.2% for Ag and Au. Since these values are very close, it is assumed that lattice mismatch does not play an important role in the differences in morphologies of the two systems.

It is important to take into account that the USP is a very fast process where all the described processes take place in micrometers' volume and in parts of seconds. For these reasons the deviations of the proposed models are possible.

Although this model was proposed to explain the formation mechanism of Au and Ag/TiO_2 core shell structures via USP, it is not just limited to this case. Previous reports [27,34,36] utilizing relative concentrations and solubilities of constituents revealed that the basic ttheory in our formation model is compatible with other techniques, such as flame spay pyrolysis and electron beam evaporation, and also to other materials' systems like bimetallic core shells. This indicates that, considering specific reaction parameters for other techniques and material properties, this model can be adjusted for other methods and materials for effective core-shell synthesis. What is also worth emphasizing is that this study proves metastable phases can be synthesized via USP, which is not possible with traditional techniques. This is promising for future studies to yield new advanced materials for various applications.

5. Conclusions

In this study, a new model that explains core-shell Ag/TiO_2 and Au/TiO_2 nanoparticles' formation mechanism by USP was proposed based on the solubility difference of the constituents and the diffusivity of the metal components through the core metal oxide. Moreover, it was assessed on Au/TiO_2 and Ag/TiO_2 experimental systems in a comparative manner. Some variations between these two systems revealed by morphological and structural investigations were explained as follows:

- While an important amount of Au was entrapped in the volume, most of the Ag was deposited on the TiO_2 surface due to the relatively higher solubility of $AgNO_3$ providing enough time for its diffusion to the core surface without reaching saturation.
- The size of the TiO_2 core hosting the Au was two-fold greater than Ag. Ag nanoparticles nucleated on the TiO_2 surface may hinder the boundary movement and growth. In the case of Au this was not that obvious due to the large amount of entrapment of Au in the TiO_2 volume.
- Due to the low melting point of $AgNO_3$, decomposition took place in the melt phase. Therefore, Ag nanoparticles exhibited a polygonal shape determined by Wulff's construction. In contrast, the surface area of minimized spherical-like Au nanoparticles was formed by the achieved precipitation.

In brief, besides those variations caused by the physical and chemical property differences of Au and Ag, the consistency of Ag/TiO_2 and Au/TiO_2 formation with the proposed model indicates that this new model is applicable for one-step USP synthesis of metal/oxide nanoparticles. This knowledge is promising to achieve good control over the USP process and increase its flexibility of application to different materials.

Acknowledgments: This study was supported by the Ministry of Education, Science and Sport, Republic of Slovenia (Program MARTINA, OP20.00369), which enabled the research with co-financing.

Author Contributions: Jelena Bogovic, Rebeka Rudolf, Bernd Friedrich conceived and designed the experiments; Jelena Bogovic performed the experiments; Gözde Alkan, Rebeka Rudolf, Bernd Friedrich analyzed the data; Darja Jenko contributed reagents/materials/analysis tools; Gözde Alkan wrote the paper.

Conflicts of Interest: The authors declare no conflict of interest.

References

1. Chaudhuri, R.G.; Paria, S. Core/shell nanoparticles: Classes, properties, synthesis mechanisms, characterization, and applications. *Chem. Rev.* **2011**, *112*, 2373–2433. [CrossRef] [PubMed]
2. Lehmhus, D.; Njuguna, J.; Paramsothy, M. Futuristic nanomaterials and composites: Part I. *JOM* **2015**, *67*, 2844–2847. [CrossRef]
3. Mohgadam, A.D.; Schultz, B.F.; Ferguson, J.B.; Omrani, E.; Rohadgi, P.; Gupta, N. Functional metal matrix composites-self-lubricating, self-healing, and nanocomposites—An outlook. *JOM* **2014**, *66*, 872–881.

4. Xu, X.; Zhou, S.; Long, J.; Wu, T.; Fan, Z. The synthesis of a core-shell photocatalyst material YF_3: Ho^{3+}@TiO_2 and investigation of its photocatalytic properties. *Materials* **2017**, *10*, 302. [CrossRef] [PubMed]
5. Li, G.; Tang, Z. Noble metal nanoparticle@metal oxide core/yolk-shell nanostructures as catalysts: Recent progress and perspective. *Nanoscale* **2014**, *6*, 3995–4011. [CrossRef] [PubMed]
6. Goesmann, H.; Feldmann, C. Nanoparticulate functional materials. *Angew. Chem. Int. Ed.* **2010**, *49*, 1362–1395. [CrossRef] [PubMed]
7. Srdic, V.; Mojic, B.; Nikolic, M.; Ognjanovic, S. Recent progress on synthesis of ceramics core/shell nanostructures. *Process. Appl. Ceram.* **2013**, *7*, 45–62. [CrossRef]
8. Chen, Z.; Wang, Z.L.; Zhan, P.; Zhang, J.H.; Zhang, W.Y.; Wang, H.T.; Ming, N.B. Preparation of metallodielectric composite particles with multishell structure. *Langmuir* **2004**, *20*, 3024–3046. [CrossRef]
9. Chong, M.N.; Jin, B.; Chow, C.W.K.; Saint, C. Recent developments in photocatalytic water treatment technology: A review. *Water Res.* **2010**, *44*, 2997–3027. [CrossRef] [PubMed]
10. Liu, N.; Prall, B.S.; Klimov, V.I. Hybrid gold/silica/nanocrystal-quantum-dot superstructures: Synthesis and analysis of semiconductor-metal interactions. *J. Am. Chem. Soc.* **2006**, *128*, 15362–15363. [CrossRef] [PubMed]
11. Kwon, S.; Fan, M.; Cooper, A.; Yang, H. Photocatalytic applications of micro- and nano-TiO_2 in environmental engineering. *Crit. Rev. Environ. Sci. Technol.* **2008**, *38*, 197–226. [CrossRef]
12. Zhang, H.; Banfield, J.F. Thermodynamic analysis of phase stability of nanocrystalline titania. *J. Mater. Chem.* **1998**, *8*, 2073–2076. [CrossRef]
13. Mansoori, G.A.; Bastamr, T.R.; Ahmadpour, A.; Eshaghi, Z. Environmental application of nanotechnology. *Annu. Rev. Nano Res.* **2008**, *2*, 1–73.
14. Dobrowlska, P.; Krajewska, A.; Gajda-Rączka, M.; Bartosewicz, B.; Nyga, P.; Jankiewicz, B.J. Application of turkevich method for gold nanoparticles sythesis to fabrication of SiO_2@Au and TiO_2@Au core-shell nanostructures. *Materials* **2015**, *8*, 2849–2862. [CrossRef]
15. Lai, X.; Clair, T.P.St.; Valden, M.; Goodman, D.W. Scanning tunneling microscopy studies of metal clusters supported on TiO_2 (110): Morphology and electronic structure. *Prog. Surf. Sci.* **1998**, *59*, 25–52. [CrossRef]
16. Cosandey, F.; Madey, T.E. Growth, morphology, interfacial effects and catalytic properties of Au on TiO_2. *Surf. Rev. Lett.* **2001**, *8*, 73–93. [CrossRef]
17. Vittadini, A.; Selloni, A. Small gold clusters on stoichiometric and defected TiO_2 anatase (101) and their interaction with CO: A density functional study. *J. Chem. Phys.* **2002**, *117*, 353–361. [CrossRef]
18. Koiso, M.; Palmer, B. Anisotropic surface energy. In Proceedings of the 16th OCU International Academic Symposium 2008, Osaka City University, Osaka, Japan, 15–20 December 2009; Volume 3, pp. 105–117.
19. Galhenage, R.P.; Yan, H.; Tenney, S.A.; Park, N.; Henkelman, G.; Albreth, P.; Mullins, D.R.; Chen, D.A. Understanding the nucleation and growth of metals on TiO_2: Co compared to Au, Ni, and Pt. *J. Phys. Chem. C* **2013**, *117*, 7191–7201. [CrossRef]
20. Bogovic, J.; Rudolf, R.; Friedrich, B. The controlled single-step synthesis of Ag/TiO_2 by ultrasonic spray pyrolysis (USP). *JOM* **2016**, *68*, 330–335. [CrossRef]
21. Bogovic, J.; Schwinger, A.; Stopic, S.; Friedrich, B.; Schroder, J. Controlled droplet size distribution in ultrasonic spray pyrolysis. *Metall* **2011**, *10*, 455–459.
22. Stopic, S.; Friedrich, B.; Volkov, T.; Raic, K. Mechanism and kinetics of nanosilver formation by ultrasonic spray pyrolysis—Progress report after a successful up-scaling. *Metall* **2010**, *64*, 419–426.
23. Majeric, P.; Friedrich, B.; Rudolf, R. Au-nanoparticle synthesis via ultrasonic spray pyrolysis with a separate evaporation zone. *Mater. Tehnol.* **2015**, *49*, 791–796. [CrossRef]
24. Majeric, P.; Jenko, D.; Budic, B.; Tomic, S.; Colic, M.; Friedrich, B.; Rudolf, R. Formation of non-toxic Au nanoparticles with bimodal size distribution by a modular redesign of ultrasonic spray pyrolysis. *Nanosci. Nanotechnol. Lett.* **2015**, *7*, 920–929. [CrossRef]
25. Bogovic, J.; Rudolf, R.; Majeric, P.; Stopic, S.; Jenko, D.; Budic, B.; Colic, M.; Tomic, S.; Jenko, M.; Friedrich, B. Synthesis of Au nanoparticles prepared by ultrasonic spray pyrolysis and hydrogen reduction. *Mater. Technol.* **2013**, *47*, 557–583.
26. Rudolf, R.; Friedrich, B.; Stopic, S.; Anzel, I.; Tomic, S.; Colic, M. Cytotoxicity of gold nanoparticles prepared by ultrasonic spray pyrolysis. *J. Biomater. Appl.* **2012**, *26*, 595–612. [CrossRef] [PubMed]
27. Mädler, L.; Stark, W.J.; Pratsinis, S.E. Simultaneous deposition of Au nanoparticles during flame synthesis of TiO_2 and SiO_2. *J. Mater. Res.* **2003**, *18*, 115–120. [CrossRef]

28. Teoh, W.Y. A perspective on the flame spray synthesis of photocatalyst nanoparticles. *Materials* **2013**, *6*, 3194–3212. [CrossRef] [PubMed]
29. Haugen, A.B.; Kumakiri, I.; Simon, C.; Einarsrud, M. TiO_2, TiO_2/Ag and TiO_2/Au photocatalysts prepared by spray pyrolysis. *J. Eur. Ceram. Soc.* **2011**, *31*, 291–298. [CrossRef]
30. Liu, L.G.; Bassett, W.A. Compression of Ag and phase transformation of NaCl. *J. Appl. Phys.* **1973**, *44*, 1475–1479. [CrossRef]
31. Okuyama, K.; Lenggoro, I.W. Preparation of nanoparticles via spray route. *Chem. Eng. Sci.* **2003**, *58*, 537–547. [CrossRef]
32. Tsai, S.C.; Song, Y.L.; Tsai, C.S.; Yang, C.C.; Chiu, W.Y.; Lin, H.M. Ultrasonic spray pyrolysis for nanoparticles synthesis. *J. Mater. Sci.* **2004**, *39*, 3647–3657. [CrossRef]
33. Jayanthi, G.V.; Zeng, C.S.; Messing, G.L. Modeling of solid particle formation during solution aerosol thermolysis. *Aerosol Sci. Technol.* **1993**, *19*, 478–490. [CrossRef]
34. Nomoev, A.; Bardakhanov, S.P.; Schreiber, M.; Bazarova, D.G.; Romanov, N.A.; Baldanov, B.B.; Radnaev, B.R.; Syzrantsev, V.V. Structure and mechanism of the formation of core-shell nanoparticles obtained through a one-step gas-phase synthesis by electron beam evaporation. *Beilstein J. Nanotechnol.* **2015**, *6*, 874–880. [CrossRef] [PubMed]
35. WebElements. Available online: https://www.webelements.com/compounds/gold/gold_chloride.html (accessed on 31 July 2017).
36. Deng, S.; Pingali, K.C.; Rockstraw, D.A. Synthesis of Ru-Ni core-shell nanoparticles for potential sensor applications. *IEEE Sens. J.* **2008**, *8*, 730–734. [CrossRef]
37. Zhang, H.; Banfield, J.F. Structural characteristics and mechanical and thermodynamic properties of nanocrystalline TiO_2. *Chem. Rev.* **2010**, *114*, 9613–9644. [CrossRef] [PubMed]